ACS OMEGA

http://pubs.acs.org/journal/acsodf

Article

Bismuth Coordination Polymers with Fluorinated Linkers: Aqueous Stability, Bivolatility, and Adsorptive Behavior

Alice Lulich, Mehran Amiri, Doctor Stephen, Mohammad Shohel, Zhiwei Mao, and May Nyman*

Cite This: *ACS Omega* 2023, 8, 10476−10486

Read Online

ACCESS | Metrics & More | Article Recommendations | Supporting Information

ABSTRACT: Bismuth metal−organic frameworks and coordination polymers (CP) are challenging to synthesize, given the poor solubility of bismuth precursors and asymmetric and labile ligation of Bi^{3+} due to its intrinsic lone pair. Here, we synthesize and structurally characterize three Bi^{3+}-CPs, exploiting a tetrafluoroterephtalate (F_4BDC) linker to determine the effect of high acidity on these synthesis and coordination challenges. Single-crystal X-ray diffraction characterization showed that pi−pi stacking of linkers directs framework arrangement and generally deters open porosity in the three structures, respectively featuring Bi chains (**Bi_{chain}-F_4BDC**), Bi dimers (**Bi_2-F_4BDC**) linked into chains, and Bi tetramers (**Bi_4-F_4BDC**). Powder X-ray diffraction and microscopic imaging show the high purity and stability of these compounds in water. Naphthalenedisulfonate (NDS) was used as a mineralizer in the synthesis of (**Bi_{chain}-F_4BDC**) and (**Bi_4-F_4BDC**), and studies of its role in assembly pathways yielded two additional structures featuring mixed NDS and F_4BDC, respectively, linking monomer and octamer Bi nodes, and confirmed that F_4BDC is the preferred (less labile) linker. Methylene blue (MB) adsorption studies show differing efficacies of the three Bi-F_4BDC phases, attributed to surface characteristics of the preferential growth facets, while generally most effective adsorption is attributed to the hydrophobicity of fluorinated ligands. Finally, thermogravimetric analysis of all three Bi-F_4BDC phases indicates simultaneous ligand degradation and in situ formation of volatile Bi compounds, which could be exploited in the chemical vapor deposition of Bi-containing thin films.

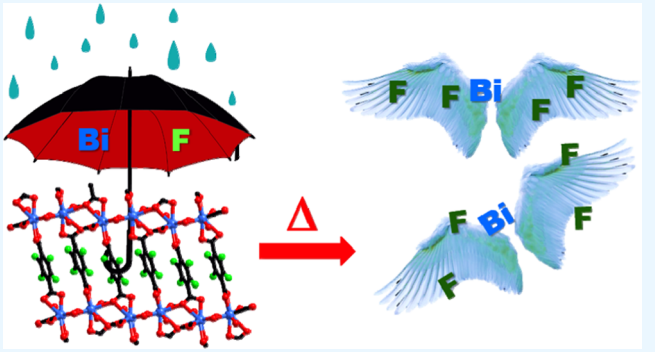

1. INTRODUCTION

Metal−organic frameworks (MOFs) and related coordination polymers (CPs) have provided a foundation for scientists to innovate many energy and environmental applications. They have versatile and tunable chemistry from modification of both the node and linker, as well as very large permanent pore spaces in some cases. Applications include gas separation, storage and conversions,[1−6] catalysis,[7−9] and conductivity and magnetism,[10−12] to name a few. Trivalent and tetravalent metal nodes are composed of some of the most stable and widely used MOFs, i.e., Cr^{III},[13,14] Ln^{III},[15,16] and $Ti/Zr/Hf^{IV}$,[17−22] due to the relative stability of the bond connecting the linker (usually carboxylate) and the node.

Bismuth (Bi^{3+}) is a high-valent metal whose MOFs/CPs are far less studied due to synthetic challenges. The insolubility of bismuth oxide in conditions conducive to forming organic−inorganic networks is one challenge. In addition, the intrinsic lone pair effect promotes the formation of long (i.e., labile) bonds between Bi^{3+} and ligands due to electron−electron repulsion. On the other hand, bismuth is biocompatible and absorbs light in the UV range. Studies of Bi-MOFs/CPs exploiting these properties benchmark drug delivery,[23,24] medical imaging,[25] photocatalytic water splitting,[26−28] and water/air decontamination.[29] Additionally, bismuth organic−inorganic networks have been studied for gas absorption,[30−33] photocatalytic H_2 production,[34] and luminescence.[35,36]

The adsorption and absorption properties of MOFs/CPs are often benchmarked using colored dye molecules. Dyes constitute most of the sewage from textile production, and they are mutagenic and carcinogenic. In addition to this targeted environmental focus, dyes can broadly represent aromatic (and often hydrophobic) aqueous contaminants. MOF studies of dye adsorption/absorption feature different metal−cation nodes and various linkers to remove a wide range of dye molecules. Metal nodes feature zirconium,[37−41] chromium,[42] iron,[42] titanium,[43] zinc,[39,44] and aluminum.[41]

Fluorinated MOFs/CPs linkers have been exploited to strategically target thermal stability, hydrophobicity, catalytic activity, and gas affinity.[45] Fluorous MOFs have demonstrated separation and purification of natural gas mixtures,[46,47] gas

Received: January 6, 2023
Accepted: February 27, 2023
Published: March 6, 2023

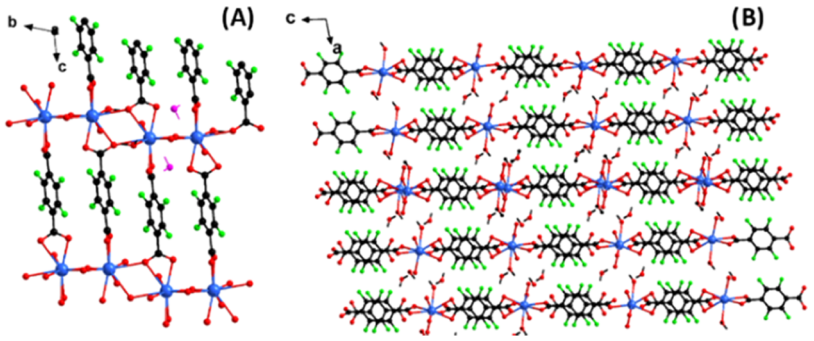

Figure 1. Views of **Bi_2-F_4BDC** down the *a*-axis (A) and *b*-axis (B). Blue is Bi, red is O, green is F, and black is C. The water molecules in (A) are shown in pink. This color code is used throughout unless indicated otherwise.

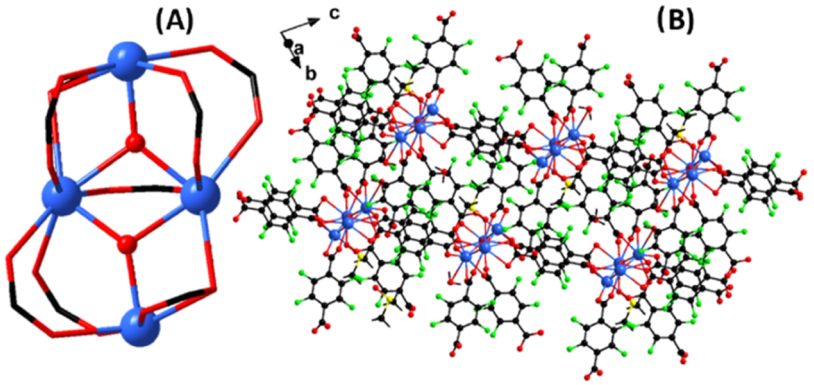

Figure 2. (A) Selected portion of the Bi_4O_2 node of **Bi_4-F_4BDC** showing the location and bonding of the eight F_4BDC linkers (COO^- only shown). (B) Representation of the **Bi_4-F_4BDC** lattice highlighting the lack of strong directionality observed in the other reported phases. The color code is the same as in Figure 1; plus yellow is sulfur of DMSO.

absorption,[47−51] oil spill cleanups,[52] dehydrating natural gas,[53] and removing hazardous wastes from water.[54]

In this study, we target the synthesis of Bi-MOFs/CPs with fluorinated linkers. We hypothesized that fluorinated linkers could provide more acidic aqueous synthesis environments to deter hydrolysis and precipitation of bismuth oxide as a competing reaction. We also expect that less labile bonds leading to more stable Bi-MOFs/CPs could be created with the electronegative F_4BDC (tetrafluorobenzenedicarboxylate) linker, a fluorinated derivative of the widely exploited terephthalate MOF linker. We present here the synthesis and characterization of three Bi-F_4BDC CPs, denoted **Bi_2-F_4BDC**, **Bi_4-F_4BDC**, and **Bi_{chain}-F_4BDC**, respectively featuring a Bi_2 node (linked into chains), a Bi_4 node, and Bi chains. Single-crystal X-ray diffraction reveals abundant $\pi-\pi$ interactions of the tetrafluorobenzene linkers, which seems to be the major driving force of crystal growth, deterring open porosity. In optimized syntheses of **Bi_4-F_4BDC** and **Bi_{chain}-F_4BDC**, 1,5-naphthalenedisulfonate (1,5-NDS) is used, presumably to aid solubility of the Bi oxide, and syntheses with reduced F_4BDC concentration produced two additional phases, featuring a Bi_1 and Bi_8 node, respectively, linked by both 1,5-NDS and F_4BDC. These studies helped clarify the role of 1,5-NDS in the assembly pathways. **Bi_2-F_4BDC**, **Bi_4-F_4BDC**, and **Bi_{chain}-F_4BDC** exhibit excellent stability, retaining their crystallinity with mechanical grinding in aqueous environments. Dye sorption (methylene blue) studies showed an efficacy ranking of **Bi_2-F_4BDC** ≫ **Bi_4-F_4BDC** > **Bi_{chain}-F_4BDC**, correlated with hydrophobicity and/or charge of exposed crystal faces of the highly crystalline compounds. Finally, in a preliminary study, thermogravimetric-differential thermal analysis (TGA-DTA) shows greater than 90% vaporization of **Bi_4-F_4BDC**, **Bi_{chain}-F_4BDC**, and **Bi_2-F_4BDC** at 300 °C. We propose a mechanism that involves simultaneous degradation of the Bi-F_4BDC coordination compounds and in situ generation of a volatile bismuth fluoride complex, potentially important for chemical vapor deposition (CVD) of bismuth-containing thin films.[55,56]

2. RESULTS AND DISCUSSION

First, we will describe here the three Bi-F_4BDC structures as determined by SCXRD (single-crystal X-ray diffraction), which were synthesized in high yields and pure forms, followed by a discussion of synthetic pathways (plus two additional minor phases) and material properties.

Bi_2-F_4BDC crystallizes in the $P\bar{1}$ space group with a unit cell volume of 849.65(5) $Å^3$ (Table S1), and the moiety formula is $[Bi_2(OH)_2(H_2O)_4(C_8F_4O_4)_2{\cdot}2(H_2O)]$. The dihydroxide-bridged Bi_2 dimer has Bi−O bond lengths of ∼2.2 Å. Each Bi is further bonded to two chelating F_4BDC ligands, one bridging F_4BDC ligand (Bi−O bond lengths ∼2.4 to 2.8 Å), and two water molecules (Bi−O bond lengths ∼2.5 to 2.7 Å). The chelating F_4BDC bridges to neighboring Bi_2 dimers in the *c*-direction through the benzene ring. The dihydroxide-bridged Bi_2 dimers are linked into chains approximately in the *b*-direction via the above-mentioned bridging F_4BDC ligand. Parallel chains of dimers are bridged by F_4BDC linkers. The rigid C_6F_4 rings are parallel with C−C separation distances of 4.3 Å and F−F separation distances of 4.4 Å. The dimer chains are not linked in the *a*-direction, and the interlayer space

https://doi.org/10.1021/acsomega.3c00114
ACS Omega 2023, 8, 10476−10486

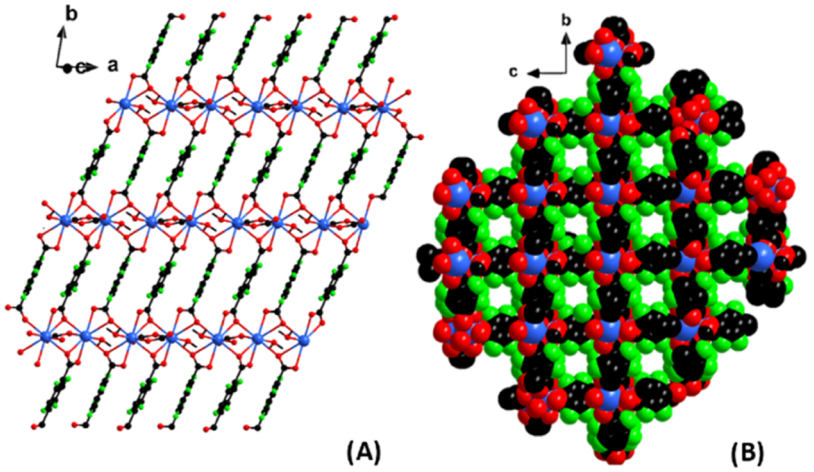

Figure 3. (A) **Bi_{chain}-F_4BDC** view emphasizing the pi−pi stacking of the F_4BDC ligands and the linking between the Bi chains in the *b*-direction. (B) View of **Bi_{chain}-F_4BDC** down the *a*-axis in space-filling representation to highlight the fluorine-lined tunnels (see Figure S2 for ball-and-stick representation of this figure). The DMSO molecules that reside in these tunnels are not shown for ease of viewing.

contains lattice waters (Figure 1) that are hydrogen-bonded to the F_4BDC oxygens.

Bi_4-F_4BDC crystallizes in the triclinic $P\bar{1}$ space group with a unit cell volume of 2091.91(5) $Å^3$ (Table S2) and a moiety formula of $[Bi_4O_2(H_2O)_2(C_8F_4O_4)_4(C_2H_6SO)\cdot 0.5(H_2O)]$. The Bi_4O_2 tetramer core has been observed prior in coordination compounds and isolated clusters.[57,58] The small cluster features a planar arrangement of four Bi and two oxo-ligands (Figure 2a). Three Bi surround each oxo in a triangle with Bi−O bond distances from 2.07 to 2.32 Å. The tetramer features seven F_4BDC ligands that straddle two Bi centers and one F_4BDC ligand that chelates one Bi and bridges to a second; Bi−O bond lengths range from 2.31 to 2.53 Å. One additional dimethyl sulfoxide (DMSO) and water molecule bind two Bi centers. A view of the Bi_4O_2 cluster plus complete ligands/linkers is shown in Figure S1. The Bi_4O_2 clusters are linked in the *bc*-plane via F_4BDC bridging through the benzene ring. Unlike the Bi chain phase discussed below and the Bi_2 phase discussed above, there is not strong directionality of the linkers driven by pi−pi stacking of the benzene rings in this rather asymmetric framework.

Bi_{chain}-F_4BDC also crystallizes in the $P\bar{1}$ space group with a unit cell volume of 849.65(5) $Å^3$ (Table S3) and a moiety formula of $[Bi(H_2O)(C_8F_4O_4)_{1.5}(C_2H_6SO)]$. Eight-coordinate Bi forms chains along the *a*-axis, and the chains are bridged by F_4BDC linkers (Figure 3a). Each Bi is chelated by two F_4BDC and bridged to its two neighboring Bi. These Bi−O bond distances range from ∼2.4 to 2.7 Å. Each Bi bonds an additional F_4-BDC in a monodentate fashion, which bridges the Bi chains in the *c*-direction, and the eighth ligand to Bi is a water molecule. A view of the *ac*-plane (Figure S2) shows that the Bi chains are zig-zag, and DMSO molecules sit between the chains in the F-lined tunnels that are discussed below. To summarize, **Bi_{chain}-F_4BDC** is linked in three dimensions, via the Bi chains in the *a*-direction and through the F_4-BDC linkers in the *b*-direction and *c*-direction. Like **Bi_2-F_4BDC**, **Bi_{chain}-F_4BDC** features pi−pi stacking of the fluorinated benzene rings with considerably closer intermolecular interaction distances: C−C = 3.4 Å and F−F = 3.1 Å along the *a*-direction. The view down the *a*-axis reveals fluorine-lined tunnels, even observable in a space-filling model (Figure 3b) with F−F distances across the tunnel ranging from ∼6 to 9 Å and adjacent intermolecular F−F distances of <3 Å.

2.1. Reaction Pathways and Material Properties. Both **Bi_{chain}-F_4BDC** and **Bi_4-F_4BDC** were synthesized with bismuth oxide as the bismuth source. This required 1,5-NDS as a mineralizer to improve the solubility of the reaction solution. We performed additional experiments to better understand the role of 1,5-NDS. Large crystals of **Bi_{chain}-F_4BDC** grow over the course of a week from a microcrystalline powder that precipitates at room temperature (Figure 4). The initial powder X-ray diffraction (PXRD) of this precipitate evidences the presence of **Bi_{chain}-F_4BDC** (major peak at 2θ = 7.86°, indicated by the red arrow, Figure 4) along with a second phase with its major diffraction peak at 2θ = 9.32° (teal arrow, Figure 4). This latter peak diminishes over 7 days of monitoring, and the final diffraction pattern shows pure **Bi_{chain}-F_4BDC**. Monitoring this transformation by microscopy imaging (Figure 4, top, for optical microscopy images, Figure S3 for additional images) initially reveals microcrystals that transform completely to the well-formed laths of **Bi_{chain}-F_4BDC**.

We were never able to obtain SCXRD data of the initial microcrystalline precipitate, but additional experiments yielded more information about this phase and parameters governing the crystallization processes of Bi-F_4BDC phases in these reaction solutions.

By decreasing F_4BDC in the reaction solution by 1/4th (see the Experimental Section), we obtained a precipitate whose PXRD is consistent with the initially precipitated microcrystalline phase, without any evidence for **Bi_{chain}-F_4BDC** (teal spectrum, Figure 4). Energy-dispersive X-ray spectroscopy (EDS) from scanning electron microscopy qualitatively shows the presence of sulfur (∼3× more than bismuth, Figure S4), while IR shows the lack of DMSO, indicating that this precipitate and any initially formed crystalline phases contain 1,5-NDS that is added as a mineralizer. EDX also shows a ∼10:1 ratio of F/Bi (Figure S4), indicating that F_4BDC is also present in the precipitate, and SEM images show a microcrystalline morphology consistent with the initial precipitate from the **Bi_{chain}-F_4BDC** synthesis (Figures S4 and S3a).

2.2. Mixed-Ligand Phases. From this precipitate, two minor phases crystallize, both containing F_4BDC and the 1,5-

https://doi.org/10.1021/acsomega.3c00114
ACS Omega 2023, 8, 10476−10486

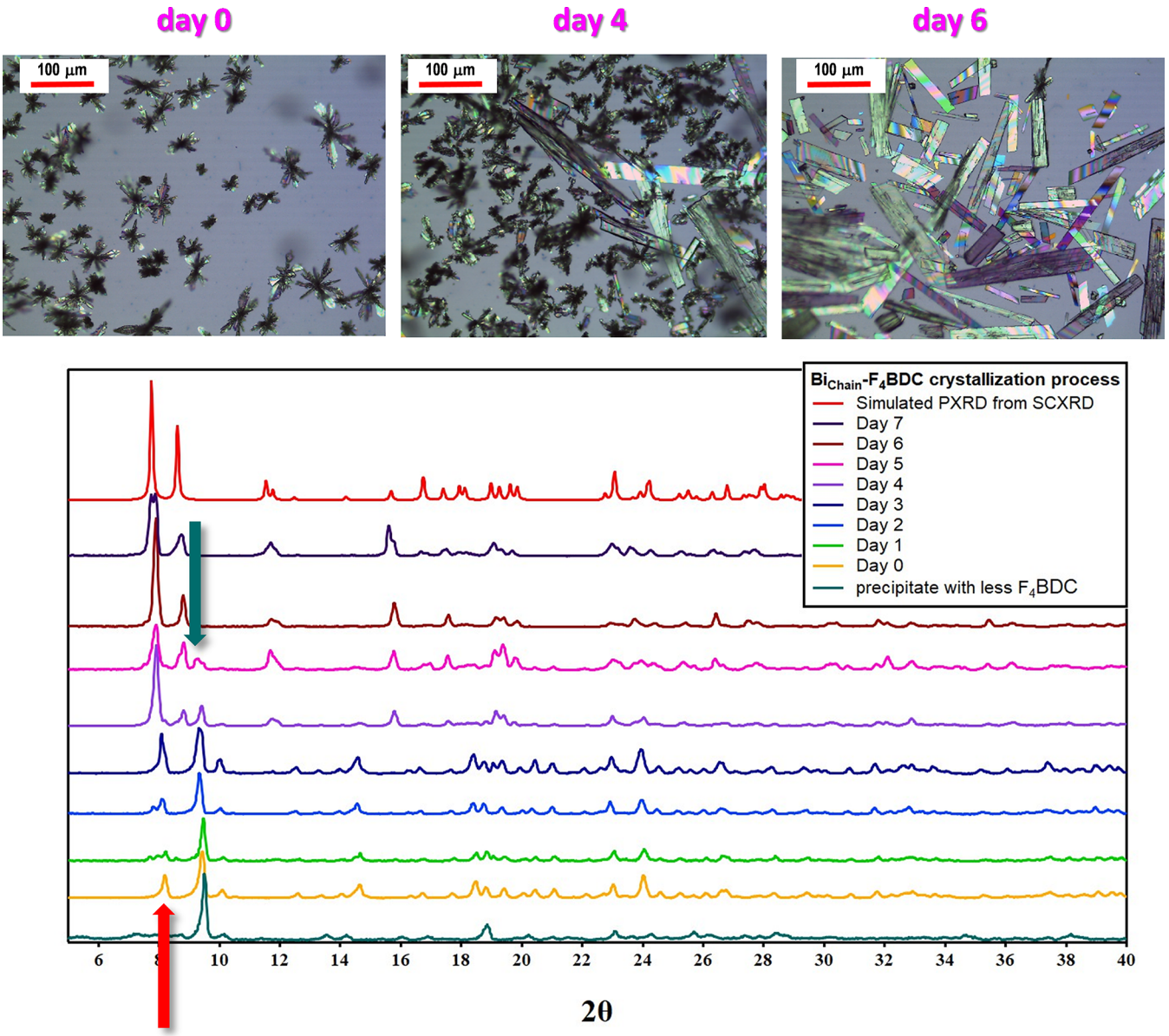

Figure 4. Bottom: PXRD showing the growth of the **Bi$_{chain}$-F$_4$BDC** phase from the initial room-temperature precipitate. Top: the evolution of microcrystals from the initial precipitate to large, well-formed crystals of **Bi$_{chain}$-F$_4$BDC**. Also see Figure S3.

NDS ligands. **Bi$_1$-F$_4$BDC-1,5-NDS** (Figure 5a and Table S4) crystallizes in the triclinic $P\bar{1}$ space group with a unit cell volume of 1396.18(3) Å^3 and a moiety formula of Bi-$(C_2H_6SO)_2(H_2O)(C_8F_4O_4H)(C_{10}H_6S_2O_6)$. Bismuth monomers are nine-coordinate, bound to one chelating F$_4$BDC, one singly bound F$_4$BDC, one chelating 1,5-NDS, and one singly bound 1,5-NDS. Bi^{3+} is further capped by two DMSO and one water molecule. For charge balance, we expect protonation of either F$_4$BDC carboxylate or 1,5-NDS, and bond valence sum (BVS, Figure S5) calculation placed the proton on the oxo of F$_4$BDC that is not bound to Bi. Rows of Bi monomers along the *a*-direction are bridged by alternating F$_4$BDC and 1,5-NDS in the perpendicular direction. Like other structures reported in this paper, there is an apparent pi−pi stacking of the parallel-aligned C_6 rings of both 1,5-NDS and F$_4$BDC linkers, with C···C distances ranging from 3.5 to 4.5 Å.

The Bi−O bonds from the F$_4$BDC ligands range from 2.33 to 2.55 Å, and the Bi−O bonds with 1,5-NDS are distinctly longer, 2.59−2.85 Å. Therefore, we expect 1,5-NDS to be more labile and weakly coordinating. Based on simulated PXRD from the single-crystal data, **Bi$_1$-F$_4$BDC-1,5-NDS** is not the initially precipitated phase shown at day 0 (Figure 4). However, we extrapolate information about the growth of **Bi$_{chain}$-F$_4$BDC** from such precipitates based on similarities of the bulk characterization. Specifically, Bi coordinated with both 1,5-NDS and F$_4$BDC initially precipitates as mixed phases from solutions containing both linkers (1:1 NDS/F$_4$BDC ratio for **Bi$_{chain}$-F$_4$BDC**; 1:0.25 NDS/F$_4$BDC ratio for **Bi$_1$-F$_4$BDC-1,5-NDS**). Next, 1,5-NDS that is more labile (based on its longer bond lengths to Bi) goes back into the solution. The precipitate becomes enriched in F$_4$BDC and crystallizes the **Bi$_{chain}$-F$_4$BDC** compound from either a solid-to-solid rearrangement process or growth at the solid−liquid interface, where the liquid contains dissolved **F$_4$BDC**. Infrared spectroscopy (FTIR) of the **Bi$_{chain}$-F$_4$BDC** precipitate also supports this. We monitored the same series of precipitate that is

https://doi.org/10.1021/acsomega.3c00114
ACS Omega 2023, 8, 10476−10486

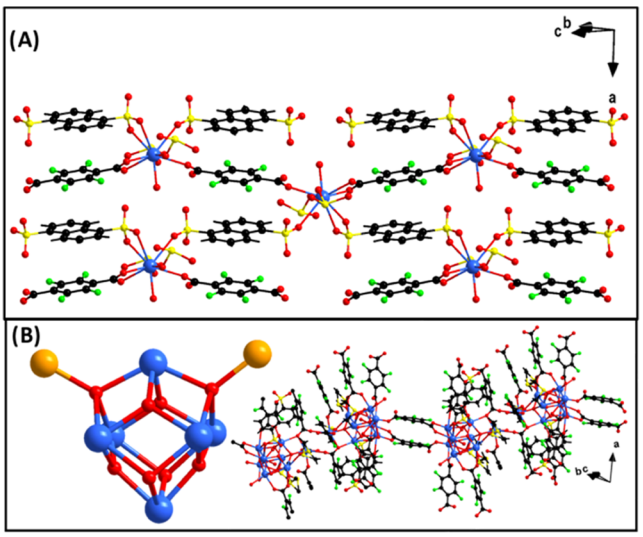

Figure 5. Two mixed-ligand phases: (A) **Bi_1-F_4BDC-1,5-NDS** and (B) **$[Bi_8]_2$-F_4BDC-1,5-NDS**. The $Bi_8O_6(OH)_2$ node highlights the common M_6 motif (blue Bi) decorated by two additional Bi (golden).

documented in Figure 4 by FTIR (Figure S6 and Table S6). In addition to the F_4BDC vibrations becoming generally sharper and better defined as **Bi_{chain}-F_4BDC** crystals grow larger, we note the ingrowth of free 1,5-NDS peaks (highlighted in Figure S6 and Table S6), consistent with the release of the weaker coordinating ligand/linker.

The second minor, mixed-ligand phase, denoted **$[Bi_8]_2$-F_4BDC-1,5-NDS** (formulated $[Bi_8O_6(OH)_2]_2(C_2H_6SO)_4(C_8F_4O_4)_{10}(C_{10}H_6S_2O_6H)$), has a fascinating arrangement, as shown in Figure 5b. This structure also demonstrates that F_4BDC is the favored linker over 1,5-NDS (6:1 F_4BDC/1,5-NDS in the lattice), despite the relative scarcity of F_4BDC in the reaction solution. In these solutions, we also expect the acidity to be less, which can yield larger nodes such as **Bi_8**. We isolated this **Bi_8** core topology recently with mixed 1,5-NDS and aminoterepthalate linkers, and it is described elsewhere.[59] In **$[Bi_8]_2$-F_4BDC-1,5-NDS**, BVS of the oxygens (Table S7 and Figure S7) identifies the Bi_8 node as $Bi_8O_6(OH)_2$. It contains the $M_6O_4(OH)_4$ core that is common to the Bi hexamer and M_4^{IV} hexamer (M = Zr, Hf, Ce, etc.) nodes and isolated clusters,[60−62] but two hydroxide protons are replaced by the two decorating Bi (Figure 5b left). Bi−O bond lengths within the Bi_6 core are ∼2.1 Å, and Bi−OH bond lengths are ∼2.4 Å. Interestingly, the μ_4-Bi_4 Bi−O bond lengths are long within the core (∼2.4 Å) and much shorter to the decorating Bi (∼2.1 Å). In this framework, Bi_8 is dimerized via bridging through the carboxylate of two F_4BDC linkers per Bi_8 pair. The $[Bi_8]_2$ units are then linked into chains (Figure 5b, right), also via two F_4BDC, but through the *trans*-carboxylates with the tetrafluorobenzene ring lying parallel to the chain direction. The dimerization is through decorating Bi of the Bi_6 core. In addition to the aforementioned four F_4BDC ligands that bridge along the chain, each Bi_8 unit is bonded to six additional F_4BDC and one 1,5-NDS. These latter seven linkers connect the chains in three dimensions in this lattice that lacks distinct tunnels or pores. Viewing down the *a*-axis reveals that the $[Bi_8]_2$ units are linked in zig-zag chains (Figure S7). For charge balance, one of the linkers must be protonated, and we assign it to the dangling S−O of 1,5-NDS (BV = 1.59, Figure S8). There are weak $\pi-\pi$ interactions between the linkers, with a few distances below ∼4 Å.

Bi_4-F_4BDC and **Bi_{chain}-F_4BDC** were obtained from identical reaction mixtures, except **Bi_{chain}-F_4BDC** crystallized at room temperature, while **Bi_4-F_4BDC** was optimally crystallized with heating at 120 °C for 2 days (see the Experimental Section). Heating at intermediate temperatures distinctly shows a mixture of the two phases (80 °C, Figure S9), implying that the low-temperature **Bi_{chain}-F_4BDC** phase transforms to the high-temperature **Bi_4-F_4BDC** phase directly, increasing the nuclearity of the Bi nodes via hydrolysis reactions. This also highlights the flexibility of the system, with labile bonds between linkers and nodes.

Routine material characterization by TGA-DTA (in air) revealed complete (90% or greater) vaporization of all three Bi-F_4BDC coordination polymers. Following these experiments, no solids remain in the alumina pan. TGA-DTA spectra for **Bi_4-F_4BDC** and **Bi_2-F_4BDC** are shown in Figures S10 and S11; **Bi_{chain}-F_4BDC** is shown in Figure 6 and discussed in detail as an example since all three are similar. Pertinent weight loss data are summarized in Table S8. The first weight loss event for **Bi_{chain}-F_4BDC** below 200 °C is ∼3%. We expect this to be a loss of DMSO, but according to the formula determined by SCXRD, this should be an 8% weight loss. This suggests that DMSO, which sits unbound in interstitial pores, evaporates from the bulk material at room temperature. We expect the fluorine-lined tunnels to not provide strong lattice interactions with the DMSO molecules, and they are readily removed without the collapse of the framework. The DTA curve corresponding with this weight loss is endothermic, as expected for the vaporization of lattice molecules, without decomposition. Starting at ∼235 °C, a rapid weight loss is initiated that ends at 305 °C (similar for all three compounds, see Figures S10 and S11). Approximately 3% of the mass remains, which decreases to 1.5% over the course of heating up to 800 °C. The initiation of this rapid weight loss is accompanied by an endothermic event, and this could be melting (the melting temperature of F_4BDC is 275 °C). Based on its formula from the X-ray structure, **Bi_{chain}-F_4BDC** is ∼31 wt % Bi (Table S8); with only 1.5% total remaining mass, the majority of Bi is volatilized. The inflection point of this rapid

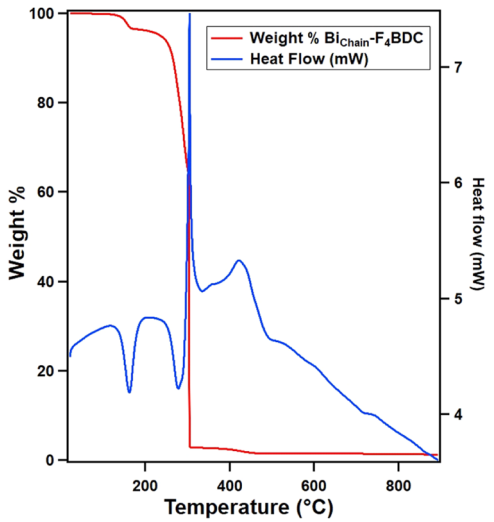

Figure 6. TGA-DSC analysis of **Bi_{chain}-F_4BDC** (see Figures S10 and S11 for **Bi_4-F_4BDC** and **Bi_2-F_4BDC**).

https://doi.org/10.1021/acsomega.3c00114
ACS Omega 2023, 8, 10476−10486

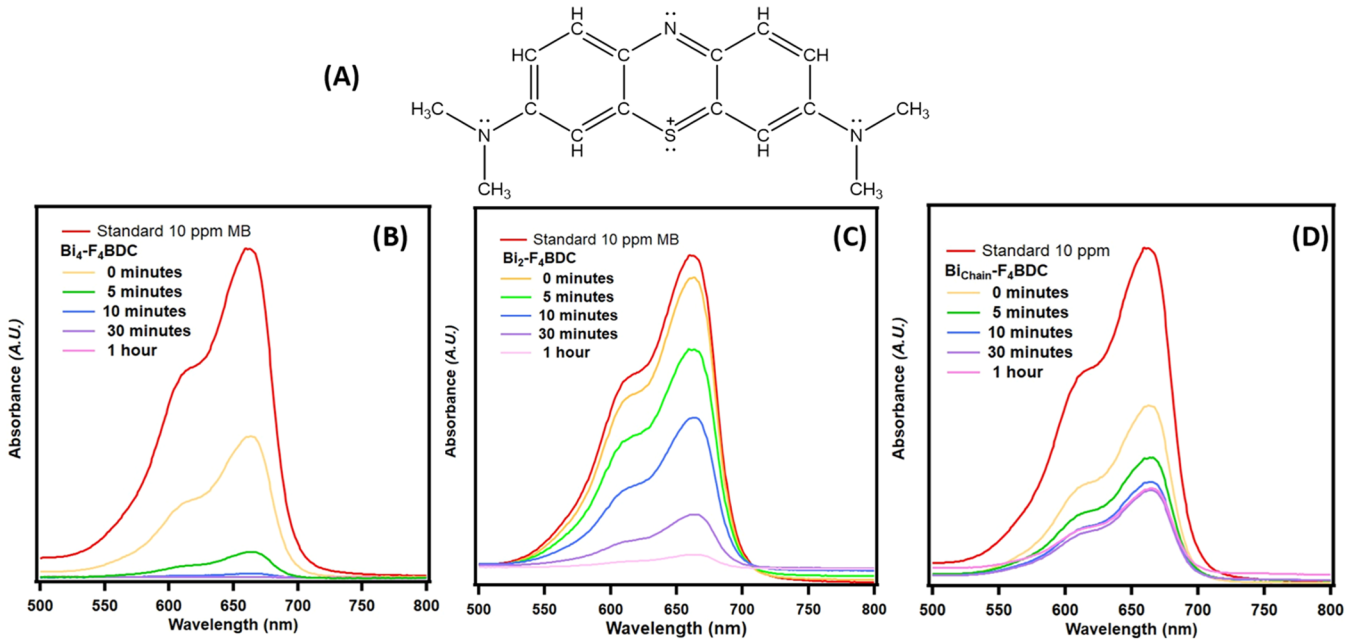

Figure 7. UV−vis spectra of the methylene blue (MB, molecule shown in part (A)) 10 ppm aqueous solution in contact with ground **Bi-F$_4$BDC** compounds, (B) **Bi$_4$-F$_4$BDC**, (C) **Bi$_2$-F$_4$BDC**, and (D) **Bi$_{chain}$-F$_4$BDC**, monitoring the removal of MB from the solution via adsorption. Analogous experiments with unground compounds are shown in Figure S13.

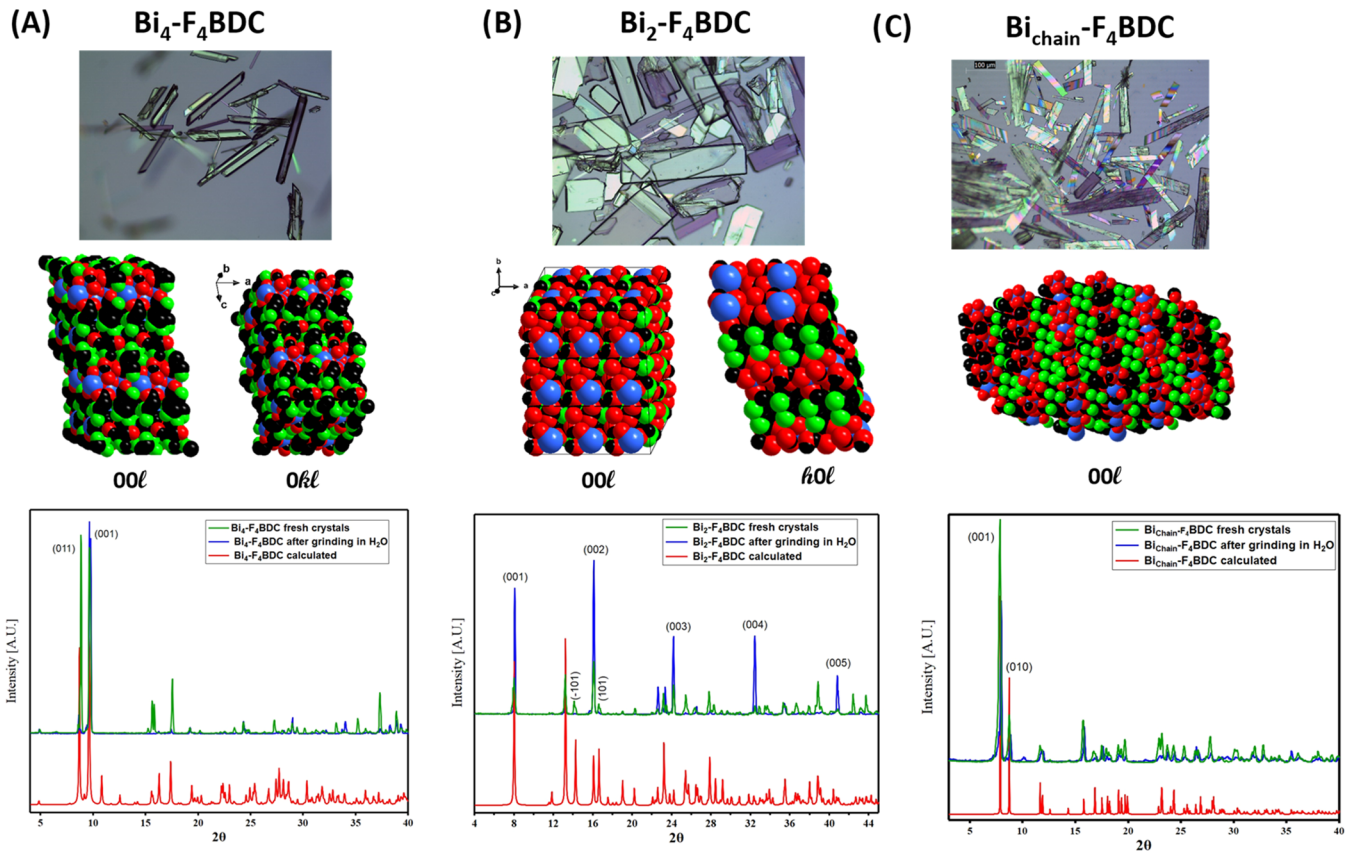

Figure 8. Microscopy images of crystals (top), space-filling representation of lattice faces with the preferred orientation (middle), and PXRD, with and without grinding in water for (A) **Bi$_4$-F$_4$BDC**, (B) **Bi$_2$-F$_4$BDC**, and (C) **Bi$_{chain}$-F$_4$BDC**, highlighting the change in the preferred orientation with physical grinding. The color code for space-filling models: blue is Bi, red is O, black is C, and green is F.

weight loss event correlates with an extremely exothermic event, which could be the decomposition of F$_4$BDC.

TGA-DSC in argon instead of air (**Bi$_2$-F$_4$BDC**, Figure S12) provided some insights into this unusual behavior of simultaneous decomposition and volatilization of metals. We

https://doi.org/10.1021/acsomega.3c00114
ACS Omega 2023, 8, 10476−10486

performed the experiment with both a slow heating rate and isotherms (Figure S12B) and the regular heating rate (10 °C/min, Figure S12A). With slow heating and isotherms, the final wt % remaining is 61%; with fast heating, the final wt % remaining is 23%, and weight is still lost at 900 °C when the experiment has concluded. The wt % Bi in **Bi_2-F_4BDC** is 41%; so again, Bi is partially volatilized with fast heating. In both experiments, the rapid decomposition/weight loss at F_4BDC at 270 °C is much diminished, and the sharp exothermic peak indicating ligand decomposition is not present. We conclude that ligand oxidation is responsible for the decomposition of F_4BDC in air, leading to complete vaporization. We were able to collect the residua for both TGA-DSC experiments in argon and measure PXRD (Figure S12C). With rapid heating, the residuum is Bi metal, likely formed by the oxidation of carbon. With slow heating, the residua are Bi_2O_3 and BiF_3, suggesting that the weight loss between 600 and 900 °C is due to the slow vaporization of BiF_3. These experiments support the hypothesis that the ligands decompose, yielding some form of BiF_3 when heated in air. Prior studies report HF as a thermolysis product of fluorocarbons.[63−65] All three compounds contain H^+ sources in hydroxyls and water, so this is a reasonable reaction pathway. Our best hypothesis then follows that Bi^{3+} is volatilized as an in situ-generated fluoride complex that differs from relatively nonvolatile BiF_3 observed in Figure S12C (reported T_v = 900 °C). Because volatile Bi precursors for chemical vapor deposition are rare,[56] we will investigate these mechanisms of Bi^{3+} vaporization in the future.

2.3. Dye Adsorption. Given the hydrophobic nature of fluorinated compounds, we compared the adsorption of dyes from aqueous solution for the three F_4BDC compounds: **Bi_{chain}-F_4BDC**, **Bi_4-F_4BDC**, and **Bi_2-F_4BDC**. Dyes serve as proxies for hydrophobic, organic material, enabling assessment of these compounds for water treatment applications or selective separations. Dye sorption studies have been used to benchmark the properties of MOFs, MOF derivatives, and other coordination compounds based on their hydrophobicity, pore volume, and surface area.[42,66,67] Methyl orange proved unstable in the self-buffering acidic media of these Bi-containing compounds, indicated by the evolution of its orange color in solution to pink, plus a shift in the maximum absorption from 466 to 510 nm. On the other hand, methylene blue (MB) proved to be stable for this study.

Based on the apparent low porosity of these materials, we expect the dye molecules to be removed from the solution via surface adsorption rather than by absorption into pores. All Bi-F_4BDC compounds were evaluated both unground and physically ground so that the particle size is roughly the same. Monitoring the initial 10 ppm MB solutions (2 mL of solution, 50 mg of each ground Bi-F_4BDC compound) by ultraviolet−visible (UV−vis) spectroscopy upon contact with the ground Bi-F_4BDC phases revealed a distinct relative adsorption rate order of **Bi_4-F_4BDC** ≫ **Bi_2-F_4BDC** > **Bi_{chain}-F_4BDC** (Figure 7). Under these conditions, **Bi_4-F_4BDC** adsorbed all of the dye in 10 min, **Bi_2-F_4BDC** adsorbed most of the dye in 1 h, and **Bi_{chain}-F_4BDC** adsorbed ∼ 70% of the dye in 1 h and did not absorb any more.

The adsorption rate improved for all three compounds with grinding, simply based on the surface area (analogous experiments without grinding are summarized in Figure S13). For **Bi_4-F_4BDC**, the rate decreased from ∼60 to 10 min for complete adsorption. For **Bi_{chain}-F_4BDC**, changes were minimal. **Bi_2-F_4BDC** showed the most dramatic improvement, from incomplete adsorption at 24 h to nearly complete adsorption at 1 h.

Characterization via PXRD (Figure 8) of the unground and ground (in a water matrix) material provided some understanding of both the trends of dye adsorption and the effect of physical grinding. All three compounds appear stable in water; the peaks remain sharp without a diminished signal/noise ratio with grinding in water. All exhibit some degree of change in peak intensity with both grinding and contact with water, and it is most prominent for **Bi_2-F_4BDC**, which also showed the greatest improvement of MB adsorption with this treatment. With grinding in water, the **Bi_2-F_4BDC** crystals show a strong preferred orientation of the (00*l*) face and a diminishment of the (*h*0*l*) orientation (Figure 8b). Normally, grinding removes the effect of the preferred orientation in PXRD analysis, so one possible interpretation (especially for **Bi_2-F_4BDC**) is the facile reorientation of the lattice in water so that more hydrophilic lattice planes are exposed to water.

Figure 8b shows space-filling models of these two aforementioned faces of the crystalline lattice. The (00*l*) orientation features Bi and O (hydrophilic), while fluorine (hydrophobic) is prominent on the (*h*0*l*) faces. This is consistent with crystal reorientation, exposing hydrophilic faces in an aqueous environment. SEM imaging of ground **Bi_2-F_4BDC** (Figure S14) reveals some mechanical shearing that the other phases do not show, most likely along the *ab*-plane, exposing the (00*l*) face shown in Figure 8b. However, why would increasing exposure to hydrophilic faces lead to more rapid adsorption of hydrophobic MB? We also need to consider the electrostatic effect on adsorption. MB is positively charged (Figure 7a), and the (00*l*) face could be negatively charged by either (1) binding and deprotonation of water to interfacial acidic Bi^{3+}, i.e., $Bi{-}OH_2 \rightarrow Bi{-}OH + H^+$, or (2) Bi^{3+} leaches out of the exposed (00*l*) surface.

Bi_4-F_4BDC shows some preferred orientations in the (00*l*) and (0*kl*) directions, which also increase with exposure to water and grinding. Both of these faces (Figure 8a) expose all of the ions present in the lattice, but most notable relative to the other phases, the aromatic carbon rings. This suggests that these crystals are hydrophobic, which can increase interaction with the dye molecules, leading to the most rapid adsorption. **Bi_{chain}-F_4BDC** has some preferred orientations of the (00*l*) face, which does not change significantly with exposure to water and grinding (Figure 8c). The (00*l*) face presents the fluorine ions. Based on this assessment, we can conclude that the favored adsorption of MB on **Bi_4-F_4BDC** is correlated with hydrophobic interaction (or pi−pi stacking) of the MB ion that features aromatic rings, while adsorption on ground **Bi_2-F_4BDC** is enhanced by the negative charge of the (00*l*) face.

Finally, we compare our MB adsorption results to MOFs with large pore volumes, which are expected to exhibit high uptake capacities. Prior-studied materials include UiO-66, ZIF-8 derivatives, and MIL-125 under a variety of conditions (see Table S9). These studies report wide-ranging values of ∼10 to 900 mg MB/g MOF.[38,40,43,44,68] ZIF-8 demonstrates the most modest values (11−16 mg MB/g ZIF-8, Table S9),[69] but also clearly demonstrated pore absorption in addition to surface adsorption. Although it is not our best-performing material, we chose to further study **Bi_2-F_4BDC** to determine its maximum adsorption capacity since it exhibits the most change in the preferred orientation and adsorption rate by physical grinding (Figures 7b, 8b, and S13b). In an experiment with 24 mL of 10 ppm MB and 50 mg of **Bi_2-F_4BDC**, ∼33% of the MB was

https://doi.org/10.1021/acsomega.3c00114
ACS Omega 2023, 8, 10476−10486

adsorbed over 8 h (Figure S21). This gives an adsorption capacity of 81 mg MB/mol **Bi_2-F_4BDC**, and we expect this to be entirely surface adsorption, given the lack of porosity. It is difficult to compare experiments in the literature with wide-ranging conditions, but **Bi_2-F_4BDC** exhibits ∼1/20th of the absorption of ZIF-8, consistent with surface-only adsorption.

3. CONCLUSIONS

Three pure crystalline coordination polymers featuring Bi^{3+} (tetramer, dimer, and chain nodes) plus fluorinated carboxylate linkers (F_4BDC) were synthesized in high yield and structurally characterized. In optimized syntheses, naphthalenedisulfunoate (NDS) was used as a mineralizer for related **Bi_{chain}-F_4BDC** and **Bi_4-F_4BDC**. By reducing the amount of F_4BDC in the reaction solution, two additional mixed-ligand CPs were obtained and structurally characterized (featuring monomer and octamer nodes, respectively). Based on this study of the **Bi_{chain}-F_4BDC** assembly process, we propose that initially, mixed-ligand phases form, but more labile NDS is eliminated via lattice rearrangement, and stable Bi-F_4BDC phases crystallize. Grinding the three Bi-F_4BDC phases in water prior to methylene blue adsorption studies does not diminish crystallinity but increases the preferred orientation, specifically **Bi_2-F_4BDC**. The preferred orientation usually decreases with mechanical grinding, but SEM images reveal "shearing" of the **Bi_2-F_4BDC** crystals, likely along the (00*l*) plane that shows considerable diffraction peak enhancement after grinding in water. Dye removal from water is most effective for **Bi_4-F_4BDC**, whose PXRD shows the least preferred orientation before and after grinding. Dye removal is significantly enhanced for **Bi_2-F_4BDC**, following mechanical grinding in water. Because the (00*l*) face exposes Bi-oxo moieties, we correlate the improved sorption with increased (00*l*) exposure to either deprotonation of bound interfacial water or leaching of Bi^{3+} into the water, leaving the surface negatively charged, increasing interaction with positively charged MB. Finally, thermogravimetric analysis of the three Bi-F_4BDC phases revealed unexpected volatility in the air at ∼300 °C, coincident with the rapid, exothermic decomposition of the F_4BDC ligands. Our hypothesis is that a fluorinated Bi compound forms in situ, which demonstrates unprecedented volatility. Future studies will include the decomposition pathway and identification of the volatile Bi compound, potentially useful for the chemical vapor deposition of Bi-containing thin-film materials.

4. EXPERIMENTAL SECTION

Materials used in the syntheses were all used as received, including tetrafluoroterephtalic acid (97%, Aldrich), bismuth(III) oxide (99.99%, Sigma Aldrich), $Bi(NO_3)_3$ (Alfa Aesar), 1,5-napthalenedisulfonic acid tetrahydrate (TCI), and dimethyl sulfoxide (DMSO 99.9%, Fisher Chemical). Millipore-filtered water with a resistance of 18.2 MΩ cm was used in all reactions.

*4.1. **Bi_2-F_4BDC** Synthesis.* A solution of bismuth nitrate was made by dissolving 1.2 g of (1.25 mmol) $Bi(NO_3)_3{\cdot}5\ H_2O$ in 10 mL of 1 M HNO_3. This mixture was stirred vigorously for 1 h, forming a clear solution with a pH of 0.85. In a separate 20 mL vial, 0.42 g of (1.8 mmol) of F_4BDC was dissolved in 16 mL of H_2O (0.84 mol). A total of 1 mL of the bismuth nitrate solution was added to 2 mL of the F_4BDC solution in a 10 mL vial. The vial was capped and left at room temperature to crystalize. After 24 h, colorless lath-shaped crystals (Figure 8b) were collected by vacuum filtration on Whatman 1 filter paper with a yield of 65% based on bismuth.

*4.2. **Bi_4-F_4BDC** Synthesis.* A solution of 1,5-naphthalenedisulfonic acid was made by dissolving 1.2 g of (4 mmol) in 8 mL of H_2O, yielding a clear solution. To this solution, 0.32 g of Bi_2O_3 (0.7 mmol) was added, and the mixture was stirred vigorously for 1 h. It turned from a bright yellow solution to a cloudy, white, concentrated mixture during this time. The pH increased from 1.63 to 2.2 upon addition of Bi_2O_3. Next, 8 mL of DMSO was added, and the mixture was heated at 80 °C in an oven for 24 h. After heating, the solution was filtered using a 0.45 mm syringe filter for use in the next step. Separately, tetrafluoroterephtalic acid (F_4BDC, 0.1 g, 0.42 mmol) was dissolved in 5 mL of H_2O. In a 10 mL vial, 1 mL of the Bi-containing solution was mixed with 2 mL of the F_4BDC solution. This gives close to a 1:1 ratio of 1,5-NDS/F_4-BDC. The vial was then placed in a sand bath and heated in an oven at 120 °C for 48 h. During the hydrothermal process, crystals of Bi_4-F_4BDC grew as well-formed rods with an estimated medium yield of around 60% based on bismuth (Figure 8a).

*4.3. **Bi_{chain}-F_4BDC** Synthesis.* Here, we followed the exact procedure for Bi_4-BDC described above, except the crystals were obtained from the evolution of a room-temperature precipitate over 7 days. The pure, needle-shaped crystals were vacuum filtered and washed with water to remove any soluble material for bulk characterization. The time study (Figure 8c) was carried out on eight parallel experiments in which the solid precipitate (that forms on day 0) was isolated (one per day) over the course of 8 days. After 8 days, needle-shaped crystals were in a pure phase with an estimated high yield of around 70% based on bismuth.

*4.4. Reduced **F_4BDC** Experiment.* Reduced **F_4BDC** experiment yielding **Bi_1-F_4BDC-1,5-NDS** and **$[Bi_8]_2$-F_4BDC-1,5-NDS** These minor phases grew out a solution/precipitate similar to that for **Bi_{chain}-F_4BDC**, except only 25% (0.5 mL) of the F_4BDC solution was added. The precipitate that forms immediately at room temperature was isolated for bulk characterization in one experiment and left in contact with the mother liquor in a duplicate experiment. Crystals of **Bi_1-F_4BDC-1,5-NDS** and **$[Bi_8]_2$-F_4BDC-1,5-NDS** were isolated from the latter (only a few crystals were observed).

4.5. Characterization. The three bulk phases **Bi_2-F_4BDC**, **Bi_4-F_4BDC**, and **Bi_{chain}-F_4BDC** were characterized by single-crystal X-ray diffraction, powder X-ray diffraction (Figures S15−S17), FTIR (Figures S18−S20), and thermogravimetric-differential thermal analysis (TGA-DTA, discussed above). Minor mixed-ligand phases were only characterized by single-crystal X-ray diffraction. All instrumentation details are provided in the Supporting Information.

4.6. Dye Sorption Studies. Dye sorption studies were executed using 10 ppm methylene (MB) solutions; further, 2 mL of the solution was placed in contact with 50 mg of each Bi-F_4BDC compound and monitored with time via UV−vis spectroscopy. Each solution was filtered before the UV−vis measurement.

■ ASSOCIATED CONTENT

Supporting Information

The Supporting Information is available free of charge at https://pubs.acs.org/doi/10.1021/acsomega.3c00114.

https://doi.org/10.1021/acsomega.3c00114
ACS Omega 2023, 8, 10476−10486

Experimental details; crystallographic information tables; supporting figures and tables including structure images, SEM images (plus EDS), photos of synthesized materials, infrared spectra, TGADTA spectra, PXRD, and BVS calculation tables (PDF)

(PDF)

Accession Codes

Crystallographic data files (cif) can be accessed from the Cambridge Crystallographic Data Center (https://www.ccdc.cam.ac.uk/structures/) by citing codes 2233822−2233824 (**Bi_2-F_4BDC**, **Bi_4-F_4BDC**, and **Bi_{chain}-F_4BDC**) and 2233976 and 2233977 (**Bi_1-F_4BDC-1,5-NDS** and **$[Bi_8]_2$-F_4BDC-1,5-NDS**).

AUTHOR INFORMATION

Corresponding Author

May Nyman − *Department of Chemistry, Oregon State University, Corvallis, Oregon 97331, United States;* orcid.org/0000-0002-1787-0518; Email: may.nyman@oregonstate.edu

Authors

Alice Lulich − *Department of Chemistry, Oregon State University, Corvallis, Oregon 97331, United States;* Present Address: Pacific Northwest National Laboratory, Richland, Washington 99354, United States

Mehran Amiri − *Department of Chemistry, Oregon State University, Corvallis, Oregon 97331, United States;* Present Address: Intel Corporation, Hillsboro, Oregon 97124, United States

Doctor Stephen − *Department of Chemistry, Oregon State University, Corvallis, Oregon 97331, United States*

Mohammad Shohel − *Department of Chemistry, Oregon State University, Corvallis, Oregon 97331, United States*

Zhiwei Mao − *Department of Chemistry, Oregon State University, Corvallis, Oregon 97331, United States*

Complete contact information is available at: https://pubs.acs.org/10.1021/acsomega.3c00114

Notes

The authors declare no competing financial interest.

ACKNOWLEDGMENTS

This study was performed at OSU, supported by the U.S. Department of Energy, Office of Basic Energy Sciences, Division of Material Sciences and Engineering, under award DE SC0010802. The authors acknowledge the Murdock Charitable Trust (grant SR-2017297) for the acquisition of the single-crystal X-ray diffractometer.

REFERENCES

(1) Daglar, H.; Gulbalkan, H. C.; Avci, G.; Aksu, G. O.; Altundal, O. F.; Altintas, C.; Erucar, I.; Keskin, S. Effect of Metal−Organic Framework (MOF) Database Selection on the Assessment of Gas Storage and Separation Potentials of MOFs. *Angew. Chem., Int. Ed.* **2021**, *60*, 7828−7837.

(2) Altintas, C.; Altundal, O. F.; Keskin, S.; Yildirim, R. Machine Learning Meets with Metal Organic Frameworks for Gas Storage and Separation. *J. Chem. Inf. Model.* **2021**, *61*, 2131−2146.

(3) Sumida, K.; Rogow, D. L.; Mason, J. A.; McDonald, T. M.; Bloch, E. D.; Herm, Z. R.; Bae, T.-H.; Long, J. R. Carbon Dioxide Capture in Metal−Organic Frameworks. *Chem. Rev.* **2012**, *112*, 724−781.

(4) Murray, L. J.; Dincă, M.; R Long, J. Hydrogen Storage in Metal−Organic Frameworks. *Chem. Soc. Rev.* **2009**, *38*, 1294−1314.

(5) McDonald, T. M.; Mason, J. A.; Kong, X.; Bloch, E. D.; Gygi, D.; Dani, A.; Crocellà, V.; Giordanino, F.; Odoh, S. O.; Drisdell, W. S.; Vlaisavljevich, B.; Dzubak, A. L.; Poloni, R.; Schnell, S. K.; Planas, N.; Lee, K.; Pascal, T.; Wan, L. F.; Prendergast, D.; Neaton, J. B.; Smit, B.; Kortright, J. B.; Gagliardi, L.; Bordiga, S.; Reimer, J. A.; Long, J. R. Cooperative Insertion of CO2 in Diamine-Appended Metal-Organic Frameworks. *Nature* **2015**, *519*, 303−308.

(6) Fan, W.; Zhang, X.; Kang, Z.; Liu, X.; Sun, D. Isoreticular Chemistry within Metal−Organic Frameworks for Gas Storage and Separation. *Coord. Chem. Rev.* **2021**, *443*, No. 213968.

(7) Horiuchi, Y.; Toyao, T.; Saito, M.; Mochizuki, K.; Iwata, M.; Higashimura, H.; Anpo, M.; Matsuoka, M. Visible-Light-Promoted Photocatalytic Hydrogen Production by Using an Amino-Functionalized Ti(IV) Metal−Organic Framework. *J. Phys. Chem. C* **2012**, *116*, 20848−20853.

(8) Palomba, J. M.; Harvey, S. P.; Kalaj, M.; Pimentel, B. R.; DeCoste, J. B.; Peterson, G. W.; Cohen, S. M. High-Throughput Screening of MOFs for Breakdown of V-Series Nerve Agents. *ACS Appl. Mater. Interfaces* **2020**, *12*, 14672−14677.

(9) Huang, Y.-B.; Liang, J.; Wang, X.-S.; Cao, R. Multifunctional Metal−Organic Framework Catalysts: Synergistic Catalysis and Tandem Reactions. *Chem. Soc. Rev.* **2017**, *46*, 126−157.

(10) Sun, L.; Campbell, M. G.; Dincă, M. Electrically Conductive Porous Metal−Organic Frameworks. *Angew. Chem., Int. Ed.* **2016**, *55*, 3566−3579.

(11) Campbell, M. G.; Sheberla, D.; Liu, S. F.; Swager, T. M.; Dincă, M. Cu3(Hexaiminotriphenylene)2: An Electrically Conductive 2D Metal−Organic Framework for Chemiresistive Sensing. *Angew. Chem., Int. Ed.* **2015**, *54*, 4349−4352.

(12) Ha, D.-G.; Wan, R.; Kim, C. A.; Lin, T.-A.; Yang, L.; Van Voorhis, T.; Baldo, M. A.; Dincă, M. Exchange Controlled Triplet Fusion in Metal−Organic Frameworks. *Nat. Mater.* **2022**, *21*, 1275−1281.

(13) Bromberg, L.; Diao, Y.; Wu, H.; Speakman, S. A.; Hatton, T. A. Chromium(III) Terephthalate Metal Organic Framework (MIL-101): HF-Free Synthesis, Structure, Polyoxometalate Composites, and Catalytic Properties. *Chem. Mater.* **2012**, *24*, 1664−1675.

(14) Henschel, A.; Gedrich, K.; Kraehnert, R.; Kaskel, S. Catalytic Properties of MIL-101. *Chem. Commun.* **2008**, *0*, 4192−4194.

(15) Zhao, S.-N.; Wang, G.; Poelman, D.; Voort, P. V. D. Luminescent Lanthanide MOFs: A Unique Platform for Chemical Sensing. *Materials* **2018**, *11*, No. 572.

(16) Sun, S.; Zhao, Y.; Wang, J.; Pei, R. Lanthanide-Based MOFs: Synthesis Approaches and Applications in Cancer Diagnosis and Therapy. *J. Mater. Chem. B* **2022**, *10*, 9535−9564.

(17) Chen, Z.; Hanna, S. L.; Redfern, L. R.; Alezi, D.; Islamoglu, T.; Farha, O. K. Reticular Chemistry in the Rational Synthesis of Functional Zirconium Cluster-Based MOFs. *Coord. Chem. Rev.* **2019**, *386*, 32−49.

(18) Abánades Lázaro, I.; Forgan, R. S. Application of Zirconium MOFs in Drug Delivery and Biomedicine. *Coord. Chem. Rev.* **2019**, *380*, 230−259.

(19) Winarta, J.; Shan, B.; Mcintyre, S. M.; Ye, L.; Wang, C.; Liu, J.; Mu, B. A Decade of UiO-66 Research: A Historic Review of Dynamic Structure, Synthesis Mechanisms, and Characterization Techniques of an Archetypal Metal−Organic Framework. *Cryst. Growth Des.* **2020**, *20*, 1347−1362.

(20) Zhu, J.; Li, P.-Z.; Guo, W.; Zhao, Y.; Zou, R. Titanium-Based Metal−Organic Frameworks for Photocatalytic Applications. *Coord. Chem. Rev.* **2018**, *359*, 80−101.

(21) Assi, H.; Mouchaham, G.; Steunou, N.; Devic, T.; Serre, C. Titanium Coordination Compounds: From Discrete Metal Complexes to Metal−Organic Frameworks. *Chem. Soc. Rev.* **2017**, *46*, 3431−3452.

(22) Yan, Y.; Li, C.; Wu, Y.; Gao, J.; Zhang, Q. From Isolated Ti-Oxo Clusters to Infinite Ti-Oxo Chains and Sheets: Recent Advances

in Photoactive Ti-Based MOFs. *J. Mater. Chem. A* **2020**, *8*, 15245−15270.
(23) Köppen, M.; Beyer, O.; Wuttke, S.; Lüning, U.; Stock, N. Synthesis, Functionalisation and Post-Synthetic Modification of Bismuth Metal-Organic Frameworks. *Dalton Trans.* **2017**, *46*, 8658−8663.
(24) Orellana-Tavra, C.; Köppen, M.; Li, A.; Stock, N.; Fairen-Jimenez, D. Biocompatible, Crystalline, and Amorphous Bismuth-Based Metal−Organic Frameworks for Drug Delivery. *ACS Appl. Mater. Interfaces* **2020**, *12*, 5633−5641.
(25) Robison, L.; Zhang, L.; Drout, R. J.; Li, P.; Haney, C. R.; Brikha, A.; Noh, H.; Mehdi, B. L.; Browning, N. D.; Dravid, V. P.; Cui, Q.; Islamoglu, T.; Farha, O. K. A Bismuth Metal−Organic Framework as a Contrast Agent for X-Ray Computed Tomography. *ACS Appl. Bio Mater.* **2019**, *2*, 1197−1203.
(26) Wang, G.; Sun, Q.; Liu, Y.; Huang, B.; Dai, Y.; Zhang, X.; Qin, X. A Bismuth-Based Metal-Organic Framework as an Efficient Visible-Light-Driven Photocatalyst. *Chem. - Eur. J.* **2015**, *21*, 2364−2367.
(27) Nguyen, V. H.; Nguyen, T. D.; Van Nguyen, T. Microwave-Assisted Solvothermal Synthesis and Photocatalytic Activity of Bismuth(III) Based Metal−Organic Framework. *Top. Catal.* **2020**, *63*, 1109−1120.
(28) Zhou, S.-M.; Ma, D.-K.; Cai, P.; Chen, W.; Huang, S.-M. TiO2/Bi2(BDC)3/BiOCl Nanoparticles Decorated Ultrathin Nanosheets with Excellent Photocatalytic Reaction Activity and Selectivity. *Mater. Res. Bull.* **2014**, *60*, 64−71.
(29) Zhao, X.; Chen, H.; Chen, X.; Hu, J.; Wu, T.; Wu, L.; Li, M. Multiple Halide Anion Doped Layered Bismuth Terephthalate with Excellent Photocatalysis for Pollutant Removal. *RSC Adv.* **2018**, *8*, 38370−38375.
(30) Grape, E. S.; Flores, J. G.; Hidalgo, T.; Martínez-Ahumada, E.; Gutiérrez-Alejandre, A.; Hautier, A.; Williams, D. R.; O'Keeffe, M.; Öhrström, L.; Willhammar, T.; Horcajada, P.; Ibarra, I. A.; Inge, A. K. A Robust and Biocompatible Bismuth Ellagate MOF Synthesized Under Green Ambient Conditions. *J. Am. Chem. Soc.* **2020**, *142*, 16795−16804.
(31) Savage, M.; Yang, S.; Suyetin, M.; Bichoutskaia, E.; Lewis, W.; Blake, A. J.; Barnett, S. A.; Schröder, M. A Novel Bismuth-Based Metal-Organic Framework for High Volumetric Methane and Carbon Dioxide Adsorption. *Chem. - Eur. J.* **2014**, *20*, 8024−8029.
(32) Thirumurugan, A.; Li, W.; Cheetham, A. K. Bismuth 2,6-Pyridinedicarboxylates: Assembly of Molecular Units into Coordination Polymers, CO2 Sorption and Photoluminescence. *Dalton Trans.* **2012**, *41*, 4126−4134.
(33) Yuan, W.-W.; Wu, J.-X.; Zhang, X.-D.; Hou, S.-Z.; Xu, M.; Gu, Z.-Y. In Situ Transformation of Bismuth Metal−Organic Frameworks for Efficient Selective Electroreduction of CO2 to Formate. *J. Mater. Chem. A* **2020**, *8*, 24486−24492.
(34) García-Sánchez, A.; Gomez-Mendoza, M.; Barawi, M.; Villar-Garcia, I. J.; Liras, M.; Gándara, F.; de la Peña O'Shea, V. A. Fundamental Insights into Photoelectrocatalytic Hydrogen Production with a Hole-Transport Bismuth Metal−Organic Framework. *J. Am. Chem. Soc.* **2020**, *142*, 318−326.
(35) Iram, S.; Imran, M.; Kanwal, F.; Iqbal, Z.; Deeba, F.; Iqbal, Q. J. Bismuth(III) Based Metal Organic Frameworks: Luminescence, Gas Adsorption, and Antibacterial Studies. *Z. Anorg. Allg. Chem.* **2019**, *645*, 50−56.
(36) Toma, O.; Allain, M.; Meinardi, F.; Forni, A.; Botta, C.; Mercier, N. Bismuth-Based Coordination Polymers with Efficient Aggregation-Induced Phosphorescence and Reversible Mechanochromic Luminescence. *Angew. Chem.* **2016**, *128*, 8130−8134.
(37) Wang, K.; Li, C.; Liang, Y.; Han, T.; Huang, H.; Yang, Q.; Liu, D.; Zhong, C. Rational Construction of Defects in a Metal−Organic Framework for Highly Efficient Adsorption and Separation of Dyes. *Chem. Eng. J.* **2016**, *289*, 486−493.
(38) Li, T.-T.; Liu, Y.-M.; Wang, T.; Wu, Y.-L.; He, Y.-L.; Yang, R.; Zheng, S.-R. Regulation of the Surface Area and Surface Charge Property of MOFs by Multivariate Strategy: Synthesis, Characterization, Selective Dye Adsorption and Separation. *Microporous Mesoporous Mater.* **2018**, *272*, 101−108.
(39) Cui, W.; Kang, X.; Zhang, X.; Cui, X. Gel-like ZnO/Zr-MOF(Bpy) Nanocomposite for Highly Efficient Adsorption of Rhodamine B Dye from Aqueous Solution. *J. Phys. Chem. Solids* **2019**, *134*, 165−175.
(40) Neshastehgar, M.; Rahmani, P.; Shojaei, A.; Molavi, H. Enhanced Adsorption Removal Performance of UiO-66 by Rational Hybridization with Nanodiamond. *Microporous Mesoporous Mater.* **2020**, *296*, No. 110008.
(41) Fan, W.; Wang, X.; Xu, B.; Wang, Y.; Liu, D.; Zhang, M.; Shang, Y.; Dai, F.; Zhang, L.; Sun, D. Amino-Functionalized MOFs with High Physicochemical Stability for Efficient Gas Storage/Separation, Dye Adsorption and Catalytic Performance. *J. Mater. Chem. A* **2018**, *6*, 24486−24495.
(42) Jiang, D.; Chen, M.; Wang, H.; Zeng, G.; Huang, D.; Cheng, M.; Liu, Y.; Xue, W.; Wang, Z. The Application of Different Typological and Structural MOFs-Based Materials for the Dyes Adsorption. *Coord. Chem. Rev.* **2019**, *380*, 471−483.
(43) Oveisi, M.; Asli, M. A.; Mahmoodi, N. M. MIL-Ti Metal-Organic Frameworks (MOFs) Nanomaterials as Superior Adsorbents: Synthesis and Ultrasound-Aided Dye Adsorption from Multi-component Wastewater Systems. *J. Hazard. Mater.* **2018**, *347*, 123−140.
(44) Hong, Y.-s.; Sun, S.; Sun, Q.; Gao, E.-Q.; Ye, M. Tuning Adsorption Capacity through Ligand Pre-Modification in Functionalized Zn-MOF Analogues. *Mater. Chem. Phys.* **2020**, *243*, No. 122601.
(45) Yang, C.; Wang, X.; Omary, M. A. Fluorous Metal−Organic Frameworks for High-Density Gas Adsorption. *J. Am. Chem. Soc.* **2007**, *129*, 15454−15455.
(46) Fan, W.; Liu, X.; Wang, X.; Li, Y.; Xing, C.; Wang, Y.; Guo, W.; Zhang, L.; Sun, D. A Fluorine-Functionalized Microporous In-MOF with High Physicochemical Stability for Light Hydrocarbon Storage and Separation. *Inorg. Chem. Front.* **2018**, *5*, 2445−2449.
(47) Liu, G.; Cadiau, A.; Liu, Y.; Adil, K.; Chernikova, V.; Carja, I.-D.; Belmabkhout, Y.; Karunakaran, M.; Shekhah, O.; Zhang, C.; Itta, A. K.; Yi, S.; Eddaoudi, M.; Koros, W. J. Enabling Fluorinated MOF-Based Membranes for Simultaneous Removal of H2S and CO2 from Natural Gas. *Angew. Chem.* **2018**, *130*, 15027−15032.
(48) Tchalala, M. R.; Bhatt, P. M.; Chappanda, K. N.; Tavares, S. R.; Adil, K.; Belmabkhout, Y.; Shkurenko, A.; Cadiau, A.; Heymans, N.; De Weireld, G.; Maurin, G.; Salama, K. N.; Eddaoudi, M. Fluorinated MOF Platform for Selective Removal and Sensing of SO2 from Flue Gas and Air. *Nat. Commun.* **2019**, *10*, No. 1328.
(49) Moghadam, P. Z.; Ivy, J. F.; Arvapally, R. K.; dos Santos, A. M.; Pearson, J. C.; Zhang, L.; Tylianakis, E.; Ghosh, P.; Oswald, I. W. H.; Kaipa, U.; Wang, X.; Wilson, A. K.; Snurr, R. Q.; Omary, M. A. Adsorption and Molecular Siting of CO2, Water, and Other Gases in the Superhydrophobic, Flexible Pores of FMOF-1 from Experiment and Simulation. *Chem. Sci.* **2017**, *8*, 3989−4000.
(50) Zhang, D.-S.; Chang, Z.; Li, Y.-F.; Jiang, Z.-Y.; Xuan, Z.-H.; Zhang, Y.-H.; Li, J.-R.; Chen, Q.; Hu, T.-L.; Bu, X.-H. Fluorous Metal-Organic Frameworks with Enhanced Stability and High H2/CO2 Storage Capacities. *Sci. Rep.* **2013**, *3*, No. 3312.
(51) Yang, C.; Wang, X.; Omary, M. A. Crystallographic Observation of Dynamic Gas Adsorption Sites and Thermal Expansion in a Breathable Fluorous Metal−Organic Framework. *Angew. Chem., Int. Ed.* **2009**, *48*, 2500−2505.
(52) Mukherjee, S.; Kansara, A. M.; Saha, D.; Gonnade, R.; Mullangi, D.; Manna, B.; Desai, A. V.; Thorat, S. H.; Singh, P. S.; Mukherjee, A.; Ghosh, S. K. An Ultrahydrophobic Fluorous Metal-Organic Framework Derived Recyclable Composite as a Promising Platform to Tackle Marine Oil Spills. *Chem. - Eur. J.* **2016**, *22*, 10937−10943.
(53) Cadiau, A.; Belmabkhout, Y.; Adil, K.; Bhatt, P. M.; Pillai, R. S.; Shkurenko, A.; Martineau-Corcos, C.; Maurin, G.; Eddaoudi, M. Hydrolytically Stable Fluorinated Metal-Organic Frameworks for Energy-Efficient Dehydration. *Science* **2017**, *356*, 731−735.

https://doi.org/10.1021/acsomega.3c00114
ACS Omega 2023, 8, 10476−10486

(54) Yuan, N.; Gong, X.-R.; Han, B.-H. Hydrophobic Fluorous Metal−Organic Framework Nanoadsorbent for Removal of Hazardous Wastes from Water. *ACS Appl. Nano Mater.* **2021**, *4*, 1576−1585.
(55) Brooks, K. C.; Turnipseed, S. B.; Barkley, R. M.; Sievers, R. E.; Tulchinsky, V.; Kaloyeros, A. E. Synthesis and Characterization of Volatile Bismuth.Beta.-Diketonate Compounds for Metal-Organic Chemical Vapor Deposition of Thin Films. *Chem. Mater.* **1992**, *4*, 912−916.
(56) Lieberman, C. M.; Wei, Z.; Filatov, A. S.; Dikarev, E. V. Mixed-Ligand Approach to Changing the Metal Ratio in Bismuth−Transition Metal Heterometallic Precursors. *Inorg. Chem.* **2016**, *55*, 3946−3951.
(57) Loera Fernandez, I. I.; Donaldson, S. L.; Schipper, D. E.; Andleeb, S.; Whitmire, K. H. Anionic Bismuth-Oxido Carboxylate Clusters with Transition Metal Countercations. *Inorg. Chem.* **2016**, *55*, 11560−11569.
(58) Andleeb, S.; Donaldson, S. L.; Schipper, D. E.; Loera Fernandez, I. I.; ud Din, I.; Whitmire, K. H. Anionic Bismuth Oxido Clusters with Pendant Silver Cations: Synthesis and Structures of [Bi4(M3-O)2(TFA)9Ag(Tol)2]2 and Bi4(M3-O)2(TFA)10-(AgPPh3)2n. *Eur. J. Inorg. Chem.* **2017**, *2017*, 1457−1463.
(59) Amiri, M.; Lulich, A.; Chiu, N. C.; Wolff, S.; Fast, D. B.; Stickle, W. F.; Stylianou, K. C.; Nyman, M. Bismuth-Polyoxocation Coordination Networks: Controlling Nuclearity and Dimension-Dependent Photocatalysis *ACS Appl. Mater. Interfaces* (in Review).
(60) Cavka, J. H.; Jakobsen, S.; Olsbye, U.; Guillou, N.; Lamberti, C.; Bordiga, S.; Lillerud, K. P. A New Zirconium Inorganic Building Brick Forming Metal Organic Frameworks with Exceptional Stability. *J. Am. Chem. Soc.* **2008**, *130*, 13850−13851.
(61) Jakobsen, S.; Gianolio, D.; Wragg, D. S.; Nilsen, M. H.; Emerich, H.; Bordiga, S.; Lamberti, C.; Olsbye, U.; Tilset, M.; Lillerud, K. P. Structural Determination of a Highly Stable Metal-Organic Framework with Possible Application to Interim Radioactive Waste Scavenging: Hf-UiO-66. *Phys. Rev. B* **2012**, *86*, No. 125429.
(62) Lammert, M.; Wharmby, M. T.; Smolders, S.; Bueken, B.; Lieb, A.; Lomachenko, K. A.; Vos, D. D.; Stock, N. Cerium-Based Metal Organic Frameworks with UiO-66 Architecture: Synthesis, Properties and Redox Catalytic Activity. *Chem. Commun.* **2015**, *51*, 12578−12581.
(63) McEwen, W. E.; DeMassa, J. W. Acid Generation in the Thermal Decomposition of Diaryliodonium Salts. *Heteroat. Chem.* **1996**, *7*, 349−354.
(64) Burgess, D. R.; Zachariah, M. R.; Tsang, W.; Westmoreland, P. R. Thermochemical and Chemical Kinetic Data for Fluorinated Hydrocarbons. *Prog. Energy Combust. Sci.* **1995**, *21*, 453−529.
(65) Mason, R. S.; J Parry, A.; P Milton, D. M. Proton Transfer to the Fluorine Atom in Fluorobenzene. Temperature and Pressure Dependence. *J. Chem. Soc. Faraday Trans.* **1994**, *90*, 1373−1380.
(66) Joseph, L.; Jun, B.-M.; Jang, M.; Park, C. M.; Muñoz-Senmache, J. C.; Hernández-Maldonado, A. J.; Heyden, A.; Yu, M.; Yoon, Y. Removal of Contaminants of Emerging Concern by Metal-Organic Framework Nanoadsorbents: A Review. *Chem. Eng. J.* **2019**, *369*, 928−946.
(67) Hasan, Z.; Jhung, S. H. Removal of Hazardous Organics from Water Using Metal-Organic Frameworks (MOFs): Plausible Mechanisms for Selective Adsorptions. *J. Hazard. Mater.* **2015**, *283*, 329−339.
(68) Luan Tran, B.; Chin, H.-Y.; Chang, B. K.; Chiang, A. S. T. Dye Adsorption in ZIF-8: The Importance of External Surface Area. *Microporous Mesoporous Mater.* **2019**, *277*, 149−153.
(69) Li, Y.; Zhou, K.; He, M.; Yao, J. Synthesis of ZIF-8 and ZIF-67 Using Mixed-Base and Their Dye Adsorption. *Microporous Mesoporous Mater.* **2016**, *234*, 287−292.

https://doi.org/10.1021/acsomega.3c00114
ACS Omega 2023, 8, 10476−10486